



# Influence of the oxide support reducibility on the CO<sub>2</sub> methanation over Ru-based catalysts



Jochen A.H. Dreyer<sup>a,\*</sup>, Peixin Li<sup>b</sup>, Linghai Zhang<sup>a</sup>, Gein Khai Beh<sup>a</sup>, Runduo Zhang<sup>b,\*</sup>, Patrick H.-L. Sit<sup>a</sup>, Wey Yang Teoh<sup>a</sup>

<sup>a</sup> Joint Laboratory for Energy and Environmental Catalysis, Clean Energy and Nanotechnology (CLEAN) Laboratory, School of Energy and Environment, City University of Hong Kong, Kowloon, Hong Kong Special Administrative Region

<sup>b</sup> State Key Laboratory of Chemical Resource Engineering, Beijing University of Chemical Technology, Beijing, PR China

## ARTICLE INFO

### Article history:

Received 17 March 2017

Received in revised form 24 July 2017

Accepted 2 August 2017

Available online 3 August 2017

## ABSTRACT

Catalysts consisting of 5 wt.% ruthenium dispersed on four different metal oxide supports were synthesized with single-step flame spray pyrolysis and assessed for the hydrogenation of CO<sub>2</sub>. The chosen supports covered a variety of characteristics expected to alter the catalytic performance, ranging from amphoteric and irreducible Al<sub>2</sub>O<sub>3</sub>, to amphoteric and reducible ZnO and MnO<sub>x</sub>, to basic and reducible CeO<sub>2</sub>. For the pristine metal oxide supports, the catalytic activity correlated with the oxide basicity and ZnO showed the highest CO<sub>2</sub> conversion. However, CO formation through the reverse water-gas shift reaction dominated over the CO<sub>2</sub> methanation due to a lack of H<sub>2</sub> dissociation sites. The addition of Ru created such H<sub>2</sub> dissociation sites and a significant increase in CO<sub>2</sub> conversion and CH<sub>4</sub> selectivity was observed. Combining the results of H<sub>2</sub> temperature-programmed reduction, quantitative H<sub>2</sub> and CO chemisorption, *in situ* DRIFTS, and the CO<sub>2</sub> hydrogenation reaction kinetics revealed that the Ru coverage with CO decreased with the support reducibility. For the irreducible Al<sub>2</sub>O<sub>3</sub> support, the Ru particles were quasi-saturated with CO at low temperatures and the reaction was limited by the competitive Langmuir-type co-adsorption of H<sub>2</sub>. The ZnO support lead to the lowest Ru-CO coverage associated with a weak CO adsorption and the reaction was dominated by the reverse water-gas shift reaction. CeO<sub>2</sub> showed a Ru-CO coverage in between Al<sub>2</sub>O<sub>3</sub> and ZnO, which ensured the presence of H<sub>2</sub> dissociation sites while the Ru-CO adsorption strength remained sufficiently high.

© 2017 Elsevier B.V. All rights reserved.

## 1. Introduction

Global warming due to excessive fossil fuel burning and the declining accessibility of such feedstock is fortifying the needs to secure clean and renewable energy resources [1–4]. Despite the advancement of photovoltaic and wind power technologies [5], their daily and seasonal intermittent availability remains a major obstacle, both in terms of constant energy supply and the associated infrastructures [6]. Large mismatch and fluctuations in the energy supply and demand necessitates the buffering by expensive electricity storage facilities. A promising alternative technology capable of compensating such fluctuations is the power-to-gas

(P2G) process, where excess electricity is converted to H<sub>2</sub> by electrolysis followed by the methanation of CO<sub>2</sub> (Sebastier reaction, CO<sub>2</sub> + 4H<sub>2</sub> → CH<sub>4</sub> + 2H<sub>2</sub>O) [7–9]. The advantages of CO<sub>2</sub> methanation over direct H<sub>2</sub> or electricity storage are that CH<sub>4</sub> can be readily fed into the existing natural gas infrastructure and that the greenhouse gas CO<sub>2</sub> would become a recyclable chemical feedstock [10].

The most active and chemically stable catalysts hitherto reported for CO<sub>2</sub> methanation are those based on platinum group metals (e.g., Pt, Rh, Ru, Pd) [11–14]. The initial reaction step on such catalyst is the dissociative adsorption of CO<sub>2</sub> to form adsorbed CO and O (CO<sub>2</sub> → CO\* + O\*) [15–17]. The rate-limiting cleavage of the remaining C–O bond [17,18] can take place either by direct C–O dissociation to C\* and O\* [19–21], or through the H-assisted paths to form formyl or carbonyl hydride intermediates [16,17,22,23]. Further hydrogenation to CH<sub>x</sub> and finally to CH<sub>4</sub> completes the catalytic cycle. Metal oxide supports such as Al<sub>2</sub>O<sub>3</sub> [15,24–27], CeO<sub>2</sub> [12], TiO<sub>2</sub> [17,28], and SiO<sub>2</sub> [13,18,29] are commonly encountered in methanation catalysts but the understanding of metal-support interactions and their influence on the reaction mechanism is rarely

\* Corresponding authors.

E-mail addresses: [jd766@cam.ac.uk](mailto:jd766@cam.ac.uk) (J.A.H. Dreyer), [zhangrd@mail.buct.edu.cn](mailto:zhangrd@mail.buct.edu.cn) (R. Zhang).

<sup>1</sup> Present address: Department of Chemical Engineering and Biotechnology, University of Cambridge, United Kingdom.

straightforward. Depending on the type of support, its interaction with the supported metal can potentially modify the electronic state of the active sites, e.g., Ru/ZSM-5, resulting in a weakened Ru–CO bond [13]. The strength of the Ru–CO and Ru–H bonds directly dictates the surface coverage of the adsorbed reactants and hence the CH<sub>4</sub> selectivity [8,13]. At the same time, reactive sites on the supports such as the oxygen vacancies on CeO<sub>2-x</sub> can directly dissociate CO<sub>2</sub> to CO\* [12], while MgO can react with CO<sub>2</sub> to form MgCO<sub>3</sub> that serves as a reaction intermediate [29]. These active sites ought to be situated near the active metals where H<sub>2</sub> dissociation and spillover take place to catalyze the methanation of the support-dissociated CO<sub>2</sub>.

In this paper, we aim to elucidate the effects of different metal oxide supports on the CO<sub>2</sub> methanation reaction mechanism of Ru-based catalysts. Here, the industrially-relevant flame spray pyrolysis (FSP) [30–33] is used to synthesize the supported Ru methanation catalysts. A number of metal oxide supports were included in the study, from strong Lewis acid [34] and irreducible Al<sub>2</sub>O<sub>3</sub> to amphoteric and reducible CeO<sub>2</sub> and MnO<sub>x</sub> as well as to strongly basic and reducible ZnO [34]. Through the combination of reaction kinetic studies and *in situ* diffuse-reflectance infrared Fourier transform spectroscopy (DRIFTS), the correlations between the support properties and the kinetics of CO<sub>2</sub> conversion as well as the products selectivities are reported. An in-depth understanding on the effect of supports is deemed necessary to allow better design of the CO<sub>2</sub> methanation catalysts by capitalizing on the potential synergistic metal-support interactions.

## 2. Experimental

### 2.1. One-step flame synthesis of CO<sub>2</sub> methanation catalysts

All catalysts were synthesized with a one-step flame spray pyrolysis reactor (FSP). Appropriate amounts of aluminum tri-sec-butoxide (97%, Acros), cerium(II) 2-ethylhexanoate (49% in 2-ethylhexanoic acid, Strem), manganese(II) 2-ethylhexanoate (40% in mineral spirit, Strem), and zinc(II) 2-ethylhexanoate (99%, Strem) were dissolved in a 20 vol.% acetonitrile (HPLC grade, Aldrich)/xylene (99%, Aldrich) mixture for a final metal concentration of 0.5 M. For the synthesis of Ru-containing catalyst, appropriate amounts of ruthenium acetylacetone (99%, Aldrich) were added to the solution for nominal loading of 5 wt.% Ru with respect to the products Al<sub>2</sub>O<sub>3</sub>, CeO<sub>2</sub>, Mn<sub>2</sub>O<sub>3</sub>, and ZnO. A syringe pump delivered the precursor solution to the FSP nozzle with 5 mL min<sup>-1</sup> where it was dispersed with 5 L min<sup>-1</sup> O<sub>2</sub> (pressure drop at nozzle tip 1.5 bar). The precursor droplets were ignited by a supporting flame (1.5 L min<sup>-1</sup> CH<sub>4</sub> and 3.2 L min<sup>-1</sup> O<sub>2</sub>) resulting in the primary aerosol-laden flame within which particles were formed. The particles were collected on a glassfiber filter (Whatmann GF/D, 25.7 cm) with the assistance of a vacuum pump.

### 2.2. Physicochemical characterization of CO<sub>2</sub> methanation catalysts

The temperature-programmed experiments were conducted on a Micromeritics AutoChem 2950 HP Chemisorption Analyzer connected to an external MicroStar 022 Mass Spectrometer. The catalyst was accurately weighed and placed into a quartz U-tube on top of a quartz wool plug. For the H<sub>2</sub> temperature-programmed reduction (H<sub>2</sub>-TPR), 50 mg of sample were cooled to –80 °C under 50 mL min<sup>-1</sup> Ar followed by heating to 800 °C under 50 mL min<sup>-1</sup> 5% H<sub>2</sub>/Ar with a temperature ramp of 10 °C min<sup>-1</sup>. The CO<sub>2</sub> and H<sub>2</sub> temperature-programmed desorption (CO<sub>2</sub>/H<sub>2</sub>-TPD) and CO chemisorption were measured with 100 mg of catalyst after pretreatment with 50 mL min<sup>-1</sup> of 10% H<sub>2</sub>/Ar for 1 h at 400 °C. For

the CO<sub>2</sub>-TPD the sample was cooled to 25 °C under 50 mL min<sup>-1</sup> He followed by flushing with 50 mL min<sup>-1</sup> of 10% CO<sub>2</sub>/He for 1 h. The gas stream was switched to 50 mL min<sup>-1</sup> of He for 30 min to remove weakly adsorbed CO<sub>2</sub> followed by heating to 800 °C at a temperature ramp of 10 °C min<sup>-1</sup>. CO<sub>2</sub>-TPDs of pristine supports were also measured but after a pretreatment with 50 mL min<sup>-1</sup> He since no reduction of RuO<sub>x</sub> to Ru metal was required. For the H<sub>2</sub>-TPD the sample was cooled to 25 °C under 50 mL min<sup>-1</sup> of 10% H<sub>2</sub>/Ar followed by flushing with Ar at the same flowrate for 1 h to remove weakly adsorbed H<sub>2</sub>. This was followed by heating to 800 °C at 10 °C min<sup>-1</sup>. For the CO chemisorption, 50 mg of sample was cooled to –80 °C under flowing He followed by pulsing (loop volume 0.3194 mL) of 10% CO/He into the He carrier gas stream until no change in the CO peak areas was observed.

Diffuse-reflectance infrared Fourier transform spectroscopy (DRIFTS) experiments were conducted with a Tensor 27 (Bruker) equipped with a liquid N<sub>2</sub> cooled MCT detector and an *in situ* DRIFTS cell (Harrick Scientific). The average of 62 scans (corresponding to 30 s) is reported with a resolution of 8 cm<sup>-1</sup>. The basic sites of the pristine supports were probed by pretreating the pristine supports with 200 mL min<sup>-1</sup> He at 350 °C for 10 min followed by cooling to 20 °C. Once the signal stabilized the background was recorded and 2 mL min<sup>-1</sup> CO<sub>2</sub> were introduced at *t* = 0. Spectra were collected every 30 s until no changes in the signal were observed. CO<sub>2</sub> adsorption on supported Ru samples were recorded with identical parameters but after a 10% H<sub>2</sub>/He pretreatment. Once the CO<sub>2</sub> adsorption was completed, 6.4 mL min<sup>-1</sup> H<sub>2</sub> were added to the gas stream ( $\lambda$  of 0.8; see Eq. (2)). Next, the CO<sub>2</sub> flow was increased to 4 mL min<sup>-1</sup> ( $\lambda$  of 0.4) after which it was removed from the H<sub>2</sub>/He flow. Again, spectra were recorded every 30 s to monitor the removal and hydrogenation of carbon species adsorbed on the catalyst.

The morphology of the catalysts was characterized with transmission electron microscopy (Philips CM-20). X-ray diffraction (XRD) patterns were recorded with a PANalytical X'Pert3 at a scanning speed of 0.1° s<sup>-1</sup> and step size of 0.026° to identify the crystal structure of the samples. The instrument was equipped with a PIX-Cel 1D detector and the Cu K<sub>α</sub> radiation was produced at 40 kV and 40 mA. The crystal phases were identified with X'Pert Highscore Plus.

### 2.3. Assessment of CO<sub>2</sub> methanation catalysts

All catalytic experiments were conducted in a quartz tube fix bed reactor (I.D. = 5 mm, GHSV = 7640 h<sup>-1</sup>) containing 20 mg of as-synthesized catalyst diluted in 0.4 g silicon carbide (Aldrich, 200–450 mesh particle size). The sample was pretreated at 400 °C for 1 h with 50 mL min<sup>-1</sup> of 10% H<sub>2</sub>/Ar. A K-type thermocouple was inserted into the center of the catalyst bed to monitor the reaction temperature. The gas outlet composition was measured with two online gas chromatographs (GC8A, Shimadzu) connected in series, one equipped with a flame ionization detector (FID) and another with a temperature conductivity detector (TCD). Calibrated mass flow controllers (Aalborg and Bronkhorst) at the reactor inlet delivered the gas flows of H<sub>2</sub>, CO<sub>2</sub> and Ar for an overall flow rate of 50 mL min<sup>-1</sup>. The CH<sub>4</sub> selectivity was defined as:

$$S(\%) = \frac{CH_{4,out}}{CH_{4,out} + CO_{out}} \quad (1)$$

where CH<sub>4,out</sub> and CO<sub>out</sub> are the CH<sub>4</sub> and CO concentrations at the reactor outlet, respectively. The ratio between H<sub>2</sub> and CO<sub>2</sub> was defined as:

$$\lambda = \frac{H_{2,in}}{4 \cdot CO_{2,in}} \quad (2)$$

**Table 1**

Applied space groups and bulk lattice constants of the simulated  $\text{MnO}_2$  [40],  $\text{Al}_2\text{O}_3$  [41],  $\text{CeO}_2$  [42],  $\text{ZnO}$  [43], and Ru [44]. Also shown are the parameters of the modeled metal oxide support surface.

Metal oxide	Space group	a	b	c	Modeled surface	Surface dimension	Layer thickness
–	–	Å	Å	Å	–	Å	Å
$\text{MnO}_2$	$\text{P}4/\text{mm}\text{m}$	4.40	4.40	2.87	$(110)-(4 \times 2)$	$11.5 \times 12.4$	8.7
$\text{Al}_2\text{O}_3$	$\text{P}2_1/\text{m}$	5.59	8.41	8.07	$(100)-\sqrt{2} \times \sqrt{2}$	$11.7 \times 11.7$	8.6
$\text{CeO}_2$	$\text{Fm-3m}$	5.41	5.41	5.41	$(111)-\left(2\sqrt{2} \times 3\sqrt{2}\right)$	$13.3 \times 11.5$	7.8
$\text{ZnO}$	$\text{P}6_3\text{mc}$	3.25	3.25	5.21	$(0001)-\left(4\sqrt{2} \times 2\sqrt{2}\right)$	$13.0 \times 11.3$	8.4
Ru	$\text{P}6_3/\text{mmc}$	2.71	2.71	4.28	–	–	–

based on the stoichiometry of the Sabatier reaction ( $\text{CO}_2 + 4\text{H}_2 \rightarrow \text{CH}_4 + 2\text{H}_2\text{O}$ ), where  $\text{H}_{2,\text{in}}$  and  $\text{CO}_{2,\text{in}}$  are the inlet concentrations of  $\text{H}_2$  and  $\text{CO}_2$ , respectively. The  $\text{CO}_2$  conversion and  $\text{CH}_4$  selectivity were assessed between 250 and 700 °C. The  $\text{CO}_2$  conversion hereby directly reflects the reaction rate in  $\text{mol}_{\text{CO}_2} \text{ g}_{\text{Ru}}^{-1} \text{ s}^{-1}$  due to the constant Ru loading. To assure that the reaction was not limited by thermodynamics, additional measurements at 200 °C were conducted and used for calculating the activation energies.

#### 2.4. Density-functional theory (DFT) calculations

Density functional theory (DFT) [35,36] was used to study the interaction between the reaction gases  $\text{CO}_2/\text{H}_2/\text{CO}$  and the supported Ru clusters. The space groups, lattice constants, modeled surface and its dimensions, and the layer thickness of the considered metal oxide supports are listed in Table 1. A  $\text{Ru}_{19}$  cluster with an initial top surface orientation (0001) was constructed from the hexagonal Ru bulk structure and placed on the different oxide supports. Structural optimization led to stable Ru nanoparticles in the same size range as observed experimentally and with a variety of Ru edge and corner atoms. A vacuum gap of 15 Å was used to avoid interactions between periodic images.

All DFT calculations were carried out using the QUANTUM ESPRESSO package [37]. Spin-polarized calculations were conducted using the Perdew-Burke-Ernzerhof (PBE) exchange–correlation functional [38], and the ultra-soft pseudopotentials [39]. The plane wave basis sets with the kinetic energy cutoffs of 25 and 200 Ry were used for the wave functions and augmented charge density, respectively. Gamma point sampling of the reciprocal space is adequate for this system due to the large size of the supercell.

### 3. Results and discussion

#### 3.1. Catalyst synthesis and physiochemical characterization

The direct flame spray pyrolysis (FSP) of co-dissolved ruthenium acetylacetonate and the metal oxide support precursors resulted in nanoparticles of necked spherical  $\text{Ru}/\text{MnO}_x$  aggregates, spherical  $\text{Ru}/\text{Al}_2\text{O}_3$ , rhombohedral  $\text{Ru}/\text{CeO}_2$  and rod-shaped  $\text{Ru}/\text{ZnO}$  (Fig. 1). The morphologies of these Ru-loaded particles are consistent with previous work on pristine oxides synthesized with the FSP [45–51]. XRD measurements revealed the formation of  $\text{CeO}_2$ ,  $\gamma\text{-Al}_2\text{O}_3$ , and a mixture of  $\text{Mn}_2\text{O}_3$  and  $\text{Mn}_3\text{O}_4$  (Fig. S1), in agreement with literature reports of these flame-made oxides [52,53]. No Ru diffraction peaks

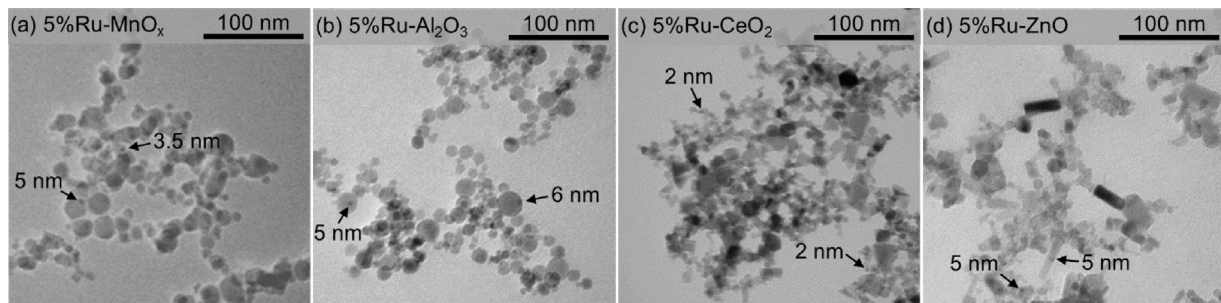


Fig. 1. TEM images of the as-synthesized (a)  $\text{Ru}/\text{MnO}_x$ , (b)  $\text{Ru}/\text{Al}_2\text{O}_3$ , (c)  $\text{Ru}/\text{CeO}_2$  and (d)  $\text{Ru}/\text{ZnO}$ . The arrows indicate possible Ru particles on the respective oxide support.

**Table 2**

Quantification of  $\text{H}_2$  consumed during  $\text{H}_2\text{-TPRs}$ ,  $\text{CO}_2$  desorbed during  $\text{CO}_2\text{-TPDs}$ , amount of CO adsorbed during CO pulsed chemisorption, and  $\text{H}_2$  desorbed during  $\text{H}_2\text{-TPDs}$ . Also shown are the estimated Ru particle sizes based on the amount of adsorbed  $\text{H}_2$ .

Catalyst <sup>a</sup>	H <sub>2</sub> consumed during TPR <sup>b</sup>	Theor. H <sub>2</sub> consumption		CO <sub>2</sub> desorbed during TPD <sup>c</sup>	CO chemisorbed <sup>d</sup>	H chemisorbed <sup>d,e</sup>	d <sub>Ru</sub> <sup>f</sup>	H <sub>ad</sub> /CO <sub>ad</sub>
		mmol <sub>H2</sub> g <sup>-1</sup>	mmol <sub>H2</sub> g <sup>-1</sup>					
$\text{Ru}/\text{MnO}_x$	5.11			0.56	0.04	0.39	1.7	10.8
$\text{Ru}/\text{Al}_2\text{O}_3$	0.73			0.23	0.11	0.09	7.1	0.83
$\text{Ru}/\text{CeO}_2$	2.75	0.99		1.25	0.12	0.42	1.6	3.4
$\text{Ru}/\text{ZnO}$	1.17			0.34	0.01	0.11	5.8	12.6

<sup>a</sup> 5 wt.% nominal Ru loading with respect to the support.

<sup>b</sup> Quantified by integrating the  $\text{H}_2\text{-TPR}$  peaks in Fig. 2.

<sup>c</sup> Quantified by integrating the  $\text{CO}_2\text{-TPD}$  peaks in Fig. 3.

<sup>d</sup> Measured through CO pulsed chemisorption after pre-reduction of catalyst with 10%  $\text{H}_2/\text{Ar}$  at 400 °C for 1 h.

<sup>e</sup> Estimated from integrating the peaks during  $\text{H}_2\text{-TPD}$ .

<sup>f</sup> Calculated from  $\text{H}_{\text{ad}}$  assuming hemispherical particle shape and Ru:H of 1.0.

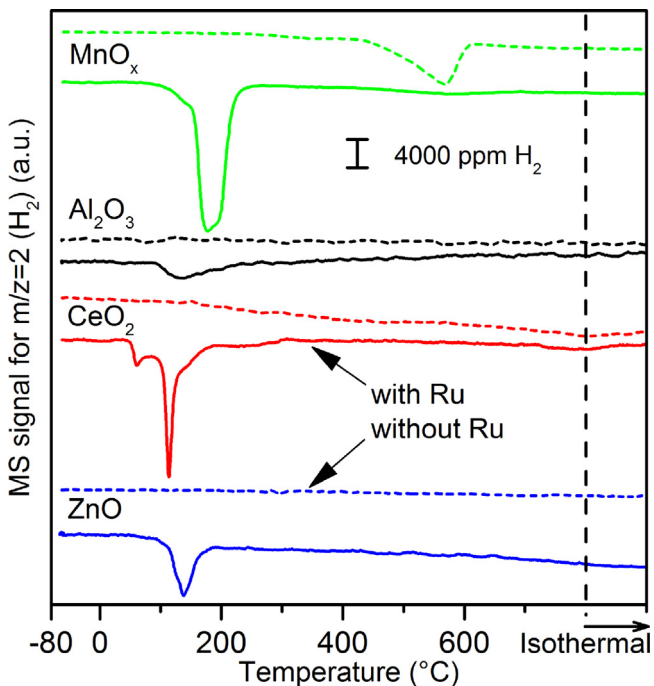


**Fig. 2.**  $\text{H}_2$  temperature-programmed reduction of the pristine metal oxides (dotted lines) and the catalysts consisting of 5% Ru supported on the respective oxides (solid lines).

were observed, in agreement with the 5 wt.% Ru loading and the small particle size deduced from the chemisorption studies (see below). The dark spots in the range of 2–6 nm (Fig. 1) might indicate Ru clusters but unambiguous identification and sizing of Ru with TEM was not possible. Gas adsorption will be discussed below as a more accurate and reliable technique to measure the Ru particle size.

Fig. 2 shows the characterization of the catalyst with  $\text{H}_2$  temperature-programmed reduction ( $\text{H}_2\text{-TPR}$ ). No reduction peak can be seen for the less reducible pristine supports, i.e.,  $\text{ZnO}$  and  $\text{Al}_2\text{O}_3$ , but upon the addition of Ru, a prominent reduction peak in between 100 and 200 °C emerged. To some extent, this low-temperature peak can be explained by the reduction of  $\text{RuO}_x$  to Ru metal. However, the  $\text{H}_2$  consumption was higher than that expected for the stoichiometric reduction of  $\text{RuO}_2$  to  $\text{Ru}^0$  (Table 2) indicating partial support reduction due to H-spillover. An exception is the  $\text{Ru}/\text{Al}_2\text{O}_3$  catalyst as can be expected for the irreducible  $\text{Al}_2\text{O}_3$ . For the highly reducible supports  $\text{CeO}_2$  and  $\text{MnO}_x$ , the amount of  $\text{H}_2$  consumption was 2.8 and 5.1 times that required for the stoichiometric  $\text{RuO}_2 \rightarrow \text{Ru}$ . The two-step reduction of  $\text{Ru}/\text{CeO}_2$  can be explained by reduction of the facets of the  $\text{CeO}_2$  rhombohedra [54–56].

The quantitative  $\text{CO}_2$  temperature-programmed desorption ( $\text{CO}_2\text{-TPD}$ ) was performed on the catalysts to measure the number of basic surface sites and their strength of basicity (Fig. 3) [57,58]. In general, only minor differences in the TPD profiles can be seen between the pristine (dotted lines) and Ru-loaded supports (solid lines) indicating that most  $\text{CO}_2$  adsorption sites exist on the oxide supports. The  $\text{Ru}/\text{ZnO}$  catalyst contains the strongest basic sites with  $\text{CO}_2$  desorption observed at 450 °C in agreement with the strong basicity reported for  $\text{ZnO}$  [34]. These basic sites typically react with the  $\text{CO}_2$  to form carbonates and formates, which speciation will be confirmed below using the DRIFTS. Despite the strength of the  $\text{ZnO}$  basicity, the amount of sites is moderate ( $0.34 \text{ mmol g}^{-1}$ ), compared to  $\text{Ru}/\text{CeO}_2$  ( $1.25 \text{ mmol g}^{-1}$ ) which is known to be a basic support [34]. Even though oxygen vacancies can be expected in the  $\text{Ru}/\text{CeO}_2$  catalyst after the  $\text{H}_2$  pretreatment

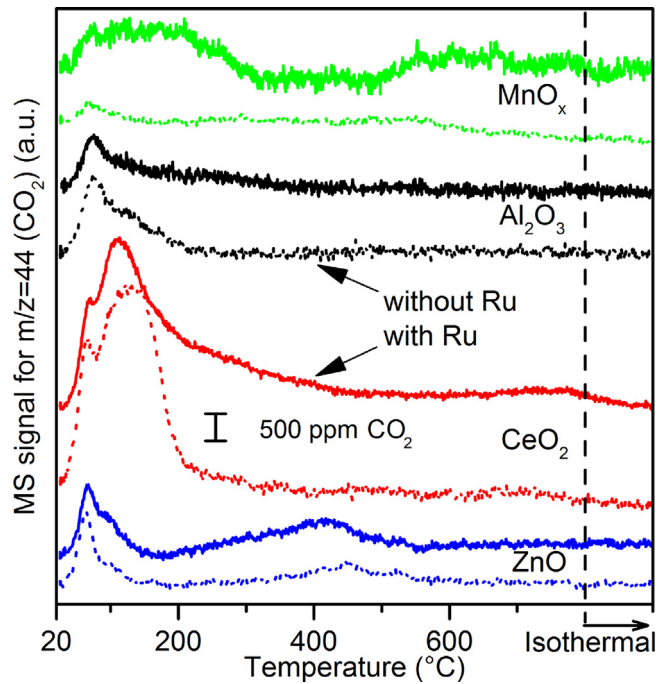


**Fig. 3.**  $\text{CO}_2$  temperature-programmed desorption of the pristine metal oxides (dotted lines) and the catalysts consisting of 5% Ru supported on the respective metal oxides (solid lines).

(1 h at 400 °C; Fig. 2), the absence of CO desorption suggests that  $\text{CO}_2$  adsorption on  $\text{CeO}_2$  vacancies was limited [59]. Only moderate  $\text{CO}_2$  desorption from the  $\text{Ru}/\text{Al}_2\text{O}_3$  ( $0.23 \text{ mmol g}^{-1}$ ) and  $\text{Ru}/\text{MnO}_x$  ( $0.56 \text{ mmol g}^{-1}$ ) sample was detected indicating little  $\text{CO}_2$  adsorption on weak basic sites.

The mode of  $\text{CO}_2$  adsorption on the supports was determined with DRIFTS (Fig. 4). The  $\text{CO}_2$  adsorption on the  $\text{Al}_2\text{O}_3$  surface shows the characteristics of bridged bicarbonates as reflected from the  $\text{O}-\text{C}-\text{O}$  symmetric ( $1434 \text{ cm}^{-1}$ ) and antisymmetric ( $1655 \text{ cm}^{-1}$ ) stretching peaks, as well as the  $\text{O}-\text{H}$  stretching at  $3624 \text{ cm}^{-1}$  and  $\text{C}-\text{O}-\text{H}$  deformation at  $1228 \text{ cm}^{-1}$  [60,61]. The bicarbonate species on these weak basic sites of  $\text{Al}_2\text{O}_3$  were formed with the surface hydroxyl groups on  $\text{Al}_2\text{O}_3$  left after the He pretreatment as indicated by the emerging valley in the OH stretching region ( $3762 \text{ cm}^{-1}$ ; Fig. 4b) [16,60]. The broad peaks in the C–O vibrational region with peak positions around  $1640$ ,  $1350$ – $1380$ , and  $1010$ – $1040 \text{ cm}^{-1}$  are likely due to the additional presence of mono- and bidentate carbonates on  $\text{Al}_2\text{O}_3$  [60,62]. The analogous bridged bicarbonate peaks of  $\text{CeO}_2$  are located at  $3621$ ,  $1650$ ,  $1408$ ,  $1216 \text{ cm}^{-1}$  along with OH consumption at  $3686 \text{ cm}^{-1}$  (Fig. 4c) [63]. The peaks at  $1625$ ,  $1245$ ,  $1014$ , and  $851 \text{ cm}^{-1}$  are assigned to bidentate carbonate while the smaller peaks at  $1533$ ,  $1339$ ,  $1058 \text{ cm}^{-1}$  are attributed to monodentate carbonate. The former is mainly accountable for the low temperature  $\text{CO}_2\text{-TPD}$  peaks at  $68$  and  $112$  °C, while the more stable structure of the latter is likely to be responsible for the tailing up to  $400$  °C [64,65]. Bridged bicarbonate peaks on  $\text{MnO}_x$  were observed at  $1639$ ,  $1408$ , and  $1274 \text{ cm}^{-1}$  (Fig. 4a). Furthermore, the  $\text{C}-\text{H}$  stretching at  $2929$  and  $2858 \text{ cm}^{-1}$  combined with the peaks at  $1543$  and  $1370 \text{ cm}^{-1}$  suggest the formation of bidentate or bridged formates [63,66]. The adsorption of  $\text{CO}_2$  on  $\text{ZnO}$  resulted in significant amounts of bicarbonate and formate formation as can be seen in the C–O–H and C–H regions at  $3730$ – $3510$  and  $2970$ – $2850 \text{ cm}^{-1}$ , respectively (Fig. 4d). Precise peaks assignment in the C–O vibrational region in case of  $\text{ZnO}$  is difficult due to the large number of overlapping peaks (Fig. 4d).

The adsorbed  $\text{H}_2$  on the Ru surface was quantified by the  $\text{H}_2\text{-TPD}$ . As tabulated in Table 2, the highest amount of chemisorbed  $\text{H}_2$

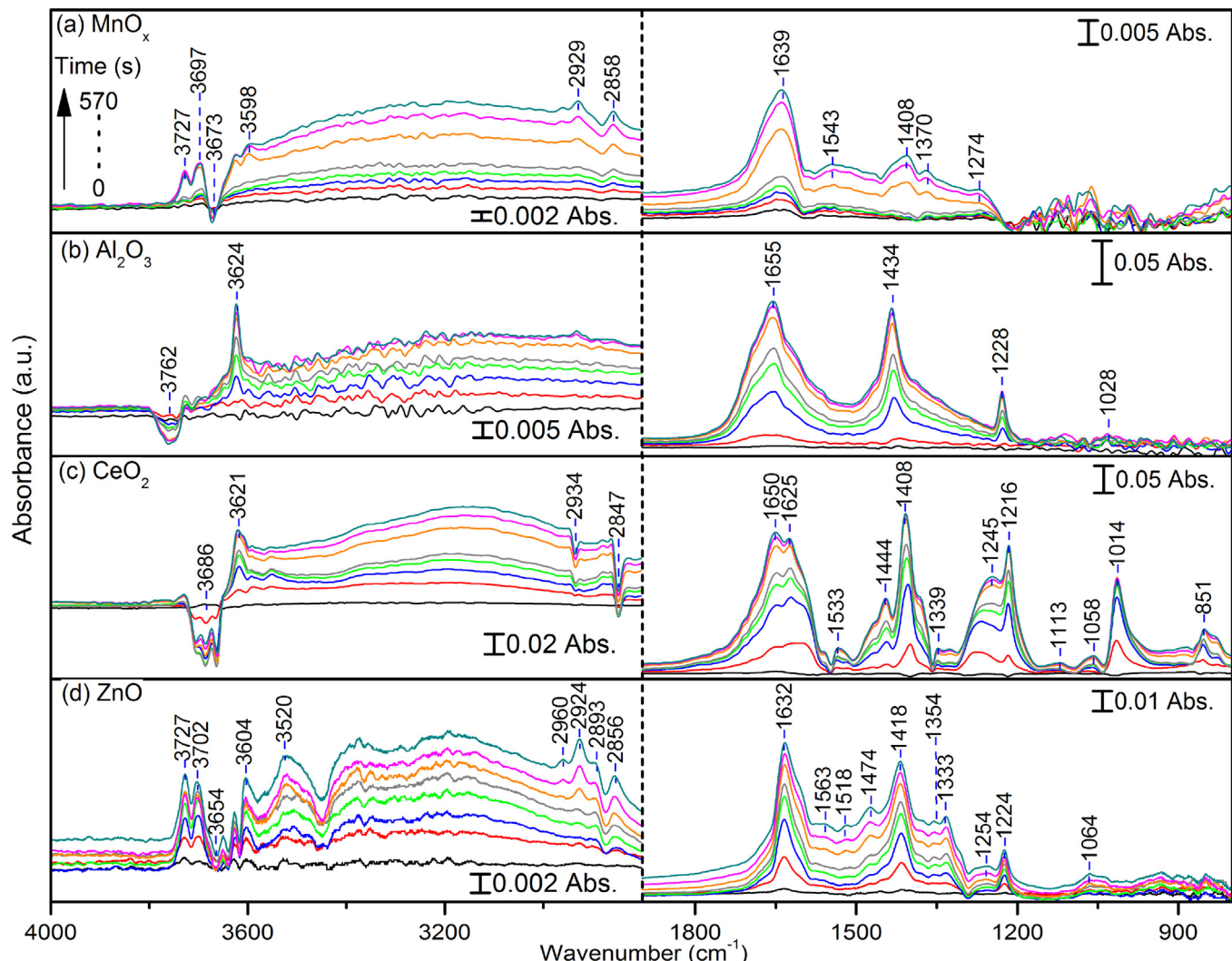


**Fig. 4.** Time-resolved DRIFT spectra in the C—H/C—O (4000–2800  $\text{cm}^{-1}$ ) and C—O vibrational range (1900–800  $\text{cm}^{-1}$ ) of pristine metal oxides of (a)  $\text{MnO}_x$ , (b)  $\text{Al}_2\text{O}_3$ , (c)  $\text{CeO}_2$  and (d)  $\text{ZnO}$ , upon the introduction of 1%  $\text{CO}_2/\text{He}$  at 20 °C.

was measured for the Ru/ $\text{CeO}_2$  sample (0.42  $\text{mmol g}^{-1}$ ) followed by Ru/ $\text{MnO}_x$  (0.39  $\text{mmol g}^{-1}$ ), Ru/ $\text{ZnO}$  (0.11  $\text{mmol g}^{-1}$ ) and Ru/ $\text{Al}_2\text{O}_3$  (0.09  $\text{mmol g}^{-1}$ ). Assuming a ratio of chemisorbed H atom to surface Ru atom of 1:1 [67], the corresponding Ru particle sizes are 1.6, 1.7, 5.8, and 7.1 nm, respectively. The calculated Ru sizes are in good qualitative agreement with the small Ru particles observed under TEM (Fig. 1) and absence of Ru peaks in the XRD (Fig. S1). CO

chemisorption was applied as an alternative technique to determine the Ru particle size (Table 2). The amount of CO chemisorbed on Ru/ $\text{Al}_2\text{O}_3$  was slightly larger than that of  $\text{H}_2$ , possibly due to carbonyl formation [68]. For the other samples however the amount of adsorbed CO was significantly lower and  $\text{H}_{\text{ad}}/\text{CO}_{\text{ad}}$  ratios of 3.4–12.6 were calculated (Table 2). A change in the number of exposed Ru sites would equally shift  $\text{H}_{\text{ad}}$  and  $\text{CO}_{\text{ad}}$  and can thus not explain the

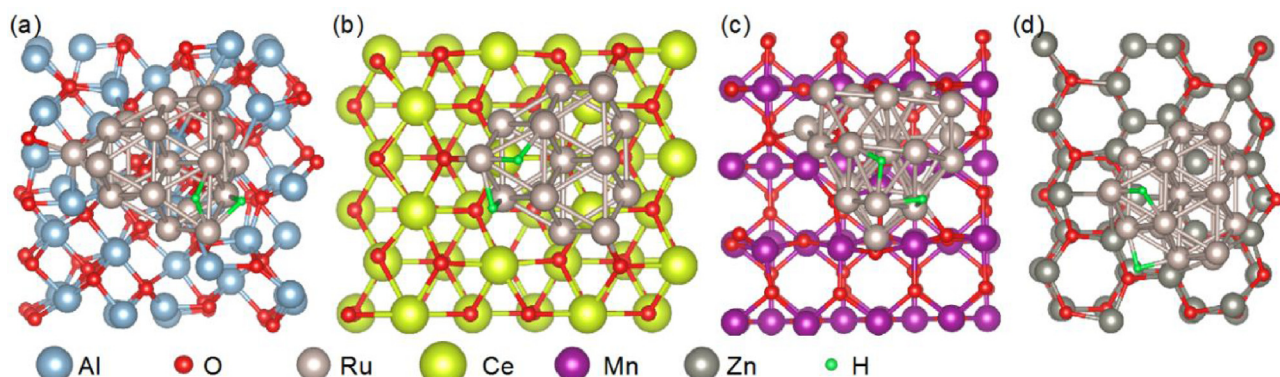


**Fig. 5.** Dissociative  $\text{H}_2$  adsorption to the Ru cluster supported on (a)  $\text{Al}_2\text{O}_3$ , (b)  $\text{CeO}_2$ , (c)  $\text{MnO}_2$ , and (d)  $\text{ZnO}$ .

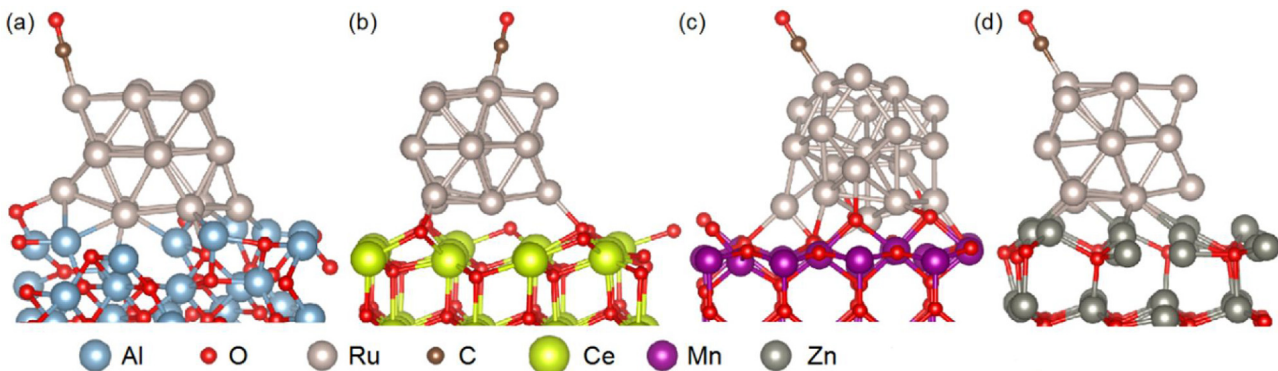


Fig. 6. CO adsorption to the Ru cluster supported on (a)  $\text{Al}_2\text{O}_3$ , (b)  $\text{CeO}_2$ , (c)  $\text{MnO}_2$ , and (d)  $\text{ZnO}$ .

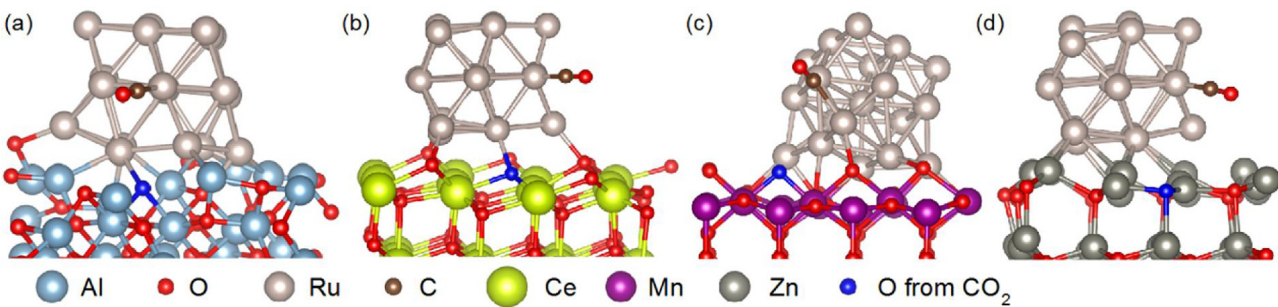


Fig. 7. Dissociative  $\text{CO}_2$  adsorption to the Ru cluster supported on (a)  $\text{Al}_2\text{O}_3$ , (b)  $\text{CeO}_2$ , (c)  $\text{MnO}_2$ , and (d)  $\text{ZnO}$ . The CO is on the Ru cluster and the O is in the vacancy on the oxide surface.

Table 3

Energies of  $\text{H}_2$  dissociative adsorption, CO adsorption and  $\text{CO}_2$  dissociative adsorption to the Ru cluster supported on  $\text{Al}_2\text{O}_3$ ,  $\text{CeO}_2$ ,  $\text{MnO}_2$ , and  $\text{ZnO}$ .

Catalyst <sup>a</sup>	$\text{H}_2$	CO	$\text{CO}_2$
	kcal/mol	kcal/mol	kcal/mol
$\text{Ru}/\text{MnO}_x$	−20.9	−50.5	−78.8
$\text{Ru}/\text{Al}_2\text{O}_3$	−24.3	−50.6	−62.5
$\text{Ru}/\text{CeO}_2$	−22.3	−49.8	−23.9
$\text{Ru}/\text{ZnO}$	−25.6	−51.3	−52.0

<sup>a</sup> 5 wt.% nominal Ru loading with respect to the support.

differences in the  $\text{H}_{\text{ad}}/\text{CO}_{\text{ad}}$  ratio. Interestingly, the  $\text{H}_{\text{ad}}/\text{CO}_{\text{ad}}$  ratios are in the sequence  $\text{Ru}/\text{Al}_2\text{O}_3 < \text{Ru}/\text{CeO}_2 < \text{Ru}/\text{MnO}_x$  and therefore follow the same order as the amount of  $\text{H}_2$  consumed during  $\text{H}_2$ -TPR. A decrease in the amount of CO adsorption on precious metals was reported to originate from a decreased electron density in the metal *d*-band upon  $\text{H}_2$  reduction of the support. Due to the decreased density, the electron back-donation from the metal *d*-band to the  $\pi^*$  anti-orbital of CO is reduced, leading to a weaker CO adsorption [69,70]. The high  $\text{H}_{\text{ad}}/\text{CO}_{\text{ad}}$  ratio of 12.6 calculated for the  $\text{Ru}/\text{ZnO}$  sample might therefore be caused by a more pronounced weakening of the CO on Ru adsorption due to the two electron reduction of  $\text{Zn}^{2+}$  to  $\text{Zn}^0$  during the  $\text{H}_2$  pretreatment.

Density functional calculations were performed to study  $\text{H}_2$  and CO adsorption on the Ru clusters. Fig. 5 and Fig. 6 show, respectively, the adsorption structures of  $\text{H}_2$  and CO on Ru/ $\text{Al}_2\text{O}_3$ , Ru/ $\text{CeO}_2$ , Ru/ $\text{MnO}_2$  and Ru/ $\text{ZnO}$ . As consistent with the experimental results, the calculated negative adsorption energies indicate that it is energetically favorable for the  $\text{H}_2$  to adsorb dissociatively. The formed chemisorbed  $\text{H}^*$  was shown to be a key intermediate in the  $\text{CO}_2$  hydrogenation mechanism [16,18]. The  $\text{H}_2$  and CO adsorption energies on Ru/ $\text{Al}_2\text{O}_3$ , Ru/ $\text{CeO}_2$ , Ru/ $\text{MnO}_2$  and Ru/ $\text{ZnO}$  are listed in Table 3. Across different metal oxide supports, the CO was consistently found to adsorb significantly stronger than the  $\text{H}_2$ . This

adsorption strength difference is a key factor in determining the  $\text{CO}_2$  methanation rate on the Ru cluster with different metal oxide supports as will be discussed in Section 3.4. A more detailed DFT study would be required to confirm the reported decreased electron density in the metal *d*-band upon reduction of the support [69,70], which is beyond the scope of this work.

As  $\text{CO}_2$  dissociation is required prior CO adsorption on Ru, DFT calculations of this process were also performed. We found that the dissociative  $\text{CO}_2$  adsorption might involve one O of the  $\text{CO}_2$  interacting with a metal oxide surface vacancy close to the Ru cluster while the CO remains on the Ru surface (Fig. 7). In the subsequent reaction steps, the hereby formed chemisorbed  $\text{CO}^*$  hydrogenates with co-adsorbed  $\text{H}^*$  as will be discussed in section 3.4.

### 3.2. Catalytic methanation of $\text{CO}_2$

The  $\text{CO}_2$  conversion and  $\text{CH}_4$  selectivity of the pristine supports and Ru containing samples are shown in Fig. 8. Notably, the trend of  $\text{CO}_2$  conversion over the pristine supports follows the strength of the support basicity as determined with  $\text{CO}_2$ -TPD, that is,  $\text{ZnO} > \text{CeO}_2 > \text{MnO}_x > \text{Al}_2\text{O}_3$  (Fig. 3). The ZnO sample with its strong basic sites was the most active sample and even reached the thermodynamic equilibrium limit at  $600^\circ\text{C}$  (Fig. 8a). Pristine  $\text{CeO}_2$  approaches the thermodynamic conversion at  $700^\circ\text{C}$ , while  $\text{MnO}_x$  and  $\text{Al}_2\text{O}_3$  only exhibited less than 20%  $\text{CO}_2$  conversion even at  $700^\circ\text{C}$ . At these high temperatures, the products are mainly CO as the reverse water-gas shift reaction (RWGS;  $\text{CO}_2 + \text{H}_2 \rightarrow \text{CO} + \text{H}_2\text{O}$ ) dominates (Fig. 8b). The addition of Ru allows the activation of the catalysts at lower temperatures and for the  $\text{CH}_4$  formation. The  $\text{CO}_2$  conversion and  $\text{CH}_4$  selectivity followed the order of  $\text{Ru}/\text{CeO}_2 > \text{Ru}/\text{Al}_2\text{O}_3 > \text{Ru}/\text{MnO}_x > \text{Ru}/\text{ZnO}$ . These samples approached the thermodynamic conversion at 350, 400, 450 and  $500^\circ\text{C}$  (Fig. 8). High  $\text{CH}_4$  selectivities (> 90%) can be obtained for the three most active catalysts at  $350^\circ\text{C}$ , beyond which the RWGS

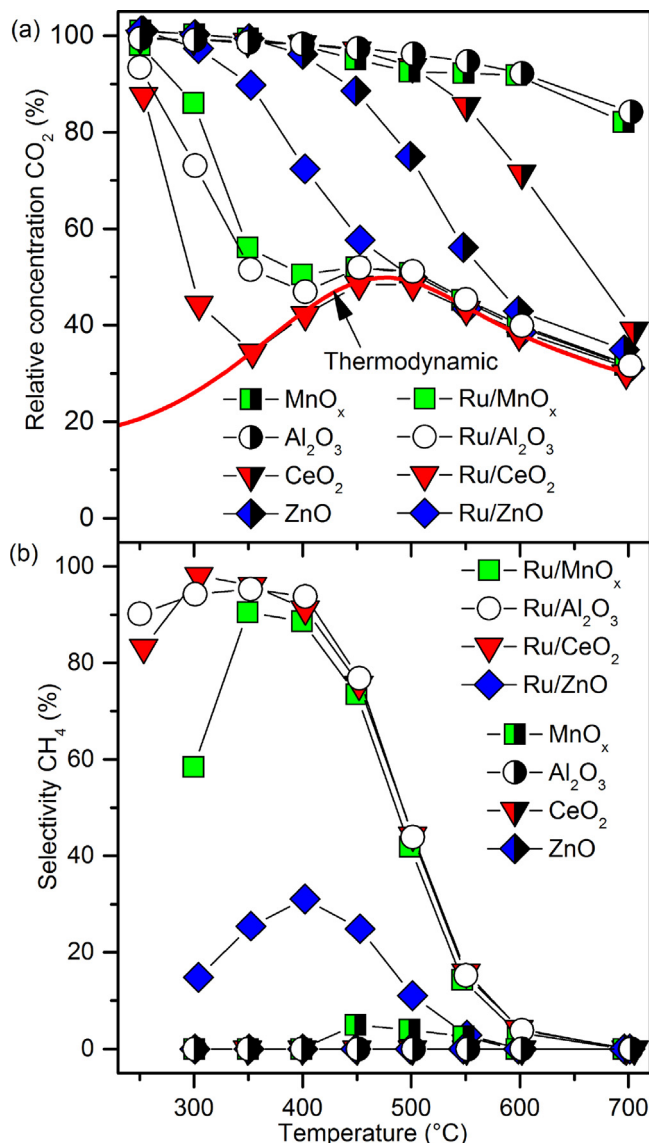


**Fig. 8.** (a) Relative CO<sub>2</sub> concentration and (b) CH<sub>4</sub> selectivity over pristine metal oxides and the catalysts consisting of 5% Ru supported on the respective metal oxides. Shown as red solid line is the thermodynamic equilibrium level calculated by minimizing the Gibbs free energy. Reactants: 2.3% CO<sub>2</sub>, 7.4% H<sub>2</sub>, balance in Ar, equivalence ratio,  $\lambda = 0.8$ ; GHSV: 7640 h<sup>-1</sup>. (For interpretation of the references to colour in this figure legend, the reader is referred to the web version of this article.)

favoring the CO production becomes significant. It is interesting to note that the CO<sub>2</sub> conversions are in qualitative agreement with the trend of CO chemisorption (see Table 2).

The Arrhenius plot in Fig. 9 reveals relatively similar apparent activation energy values,  $E_a$ , between Ru/CeO<sub>2</sub> ( $75 \pm 2$  kJ mol<sup>-1</sup>), Ru/Al<sub>2</sub>O<sub>3</sub> ( $77 \pm 2$  kJ mol<sup>-1</sup>), and Ru/MnO<sub>x</sub> ( $84 \pm 3$  kJ mol<sup>-1</sup>). These are well within the reported values of 72–105 kJ mol<sup>-1</sup> for the CO<sub>2</sub> methanation over supported Ru catalysts [20,71]. Furthermore, the values are comparable to the activation energy of CO methanation, suggesting that the initial CO<sub>2</sub> dissociation is not the limiting step [17,18]. The relatively high  $E_a$  of  $108 \pm 3$  kJ mol<sup>-1</sup> for Ru/ZnO is probably a reflection of the dominant RWGS that resulted in a low CH<sub>4</sub> selectivity (Fig. 8b). As tabulated in Table 4, the turnover frequency (TOF) is the highest for Ru/Al<sub>2</sub>O<sub>3</sub> ( $38 \cdot 10^{-2}$  s<sup>-1</sup>) followed by Ru/CeO<sub>2</sub> ( $15 \cdot 10^{-2}$  s<sup>-1</sup>), Ru/ZnO ( $6 \cdot 10^{-2}$  s<sup>-1</sup>) and Ru/MnO<sub>x</sub> ( $5 \cdot 10^{-2}$  s<sup>-1</sup>) at 300 °C and with excess H<sub>2</sub> ( $\lambda = 1.2$ ). The different TOFs corroborate the notion of a non-negligible effect of the metal oxide supports.

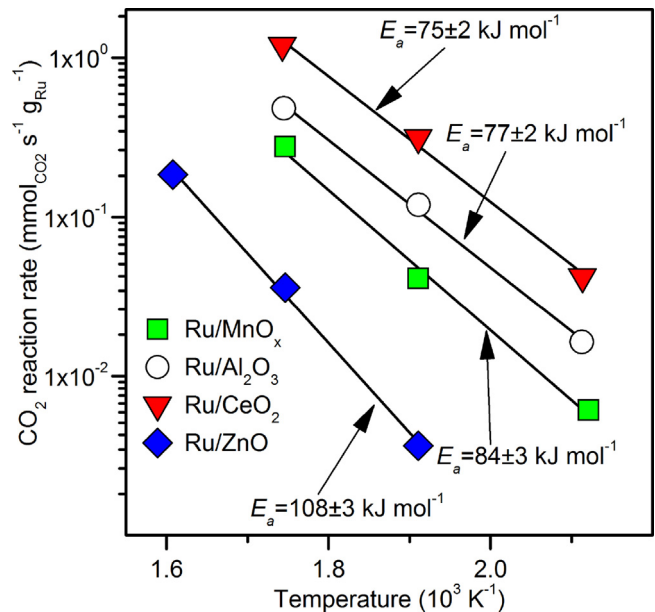


**Fig. 9.** Arrhenius plot of Ru/MnO<sub>x</sub>, Ru/Al<sub>2</sub>O<sub>3</sub>, Ru/CeO<sub>2</sub> and Ru/ZnO, and the corresponding apparent activation energies,  $E_a$ , in kJ mol<sup>-1</sup>.

**Table 4**

Turnover frequencies (TOFs) with the corresponding CO<sub>2</sub> conversion and CH<sub>4</sub> selectivity based on the rates of CO<sub>2</sub> consumption and CH<sub>4</sub>/CO production.

Catalyst <sup>a</sup>	CO <sub>2</sub> conv. %	CH <sub>4</sub> selectivity %	TOF <sub>CO2</sub> <sup>b</sup>	TOF <sub>CH4</sub> <sup>b</sup>	TOF <sub>CO</sub> <sup>b</sup>
			$10^{-2}$ , s <sup>-1</sup>	$10^{-2}$ , s <sup>-1</sup>	$10^{-2}$ , s <sup>-1</sup>
Ru/MnO <sub>x</sub>	25	90	5	5	0.5
Ru/Al <sub>2</sub> O <sub>3</sub>	32	94	38	36	2
Ru/CeO <sub>2</sub>	83	99	15	15	0.1
Ru/ZnO	1	6	6	0.4	6

<sup>a</sup> Reactor bed = 20 mg catalyst diluted in 0.4 g silicon carbide, GHSV = 7640 h<sup>-1</sup>, 22% H<sub>2</sub>, 4.6% CO<sub>2</sub>, balance in Ar, reaction temperature = 300 °C.

<sup>b</sup> Turnover frequency (TOF) calculated based on the steady state rate of CO<sub>2</sub> conversion, CH<sub>4</sub> production or CO production, and the dispersion of Ru as measured from H<sub>2</sub>-TPD.

Additional catalytic experiments were conducted as a function of H<sub>2</sub> (Fig. 10) and CO<sub>2</sub> concentration (Fig. 11). The increase in the equivalence ratio, ( $\lambda = [H_2]/[4[CO_2]]$ ), increases the CO<sub>2</sub> conversion for all catalysts (Fig. 10a), as also predicted thermodynamically. More importantly, Ru/MnO<sub>x</sub>, Ru/Al<sub>2</sub>O<sub>3</sub> and Ru/CeO<sub>2</sub> were able to attain the equilibrium conversions from relatively low temperatures of ~300 °C (Fig. 10a). Maximum CH<sub>4</sub> production rates were measured for these catalysts at 350 °C (Fig. 10b), coinciding with the onset of the endothermic RWGS reaction, after which CO production increases with increasing temperatures (Fig. 10c). The actual production rates of CH<sub>4</sub> and CO are well within the thermodynamic prediction for these three catalysts, which exhibit similar  $E_a$ . Intriguingly, the Ru/ZnO favors RWGS over CO<sub>2</sub> methanation even at the lower temperatures where the latter is expected to be dominant (Fig. 10c and Fig. 11c). This becomes evident from the higher rates of CO production than that predicted at theoretical equilibrium, at the expense of the low CH<sub>4</sub> production rates.

The dependencies of CH<sub>4</sub> production rates on H<sub>2</sub> and CO<sub>2</sub> concentrations can be better reflected from the respective log–log plots measured at sub-equilibrium levels (Fig. 12). A first order reaction with respect to the H<sub>2</sub> concentration was measured for all supported Ru catalysts, except for Ru/Al<sub>2</sub>O<sub>3</sub> ( $0.7 \pm 0.05$ ; Fig. 12a). The first order dependency is consistent with the expected rate determining step of CO\* hydrogenation [17,18]. The lower reaction order for Ru/Al<sub>2</sub>O<sub>3</sub> is likely caused by a quasi-saturation of

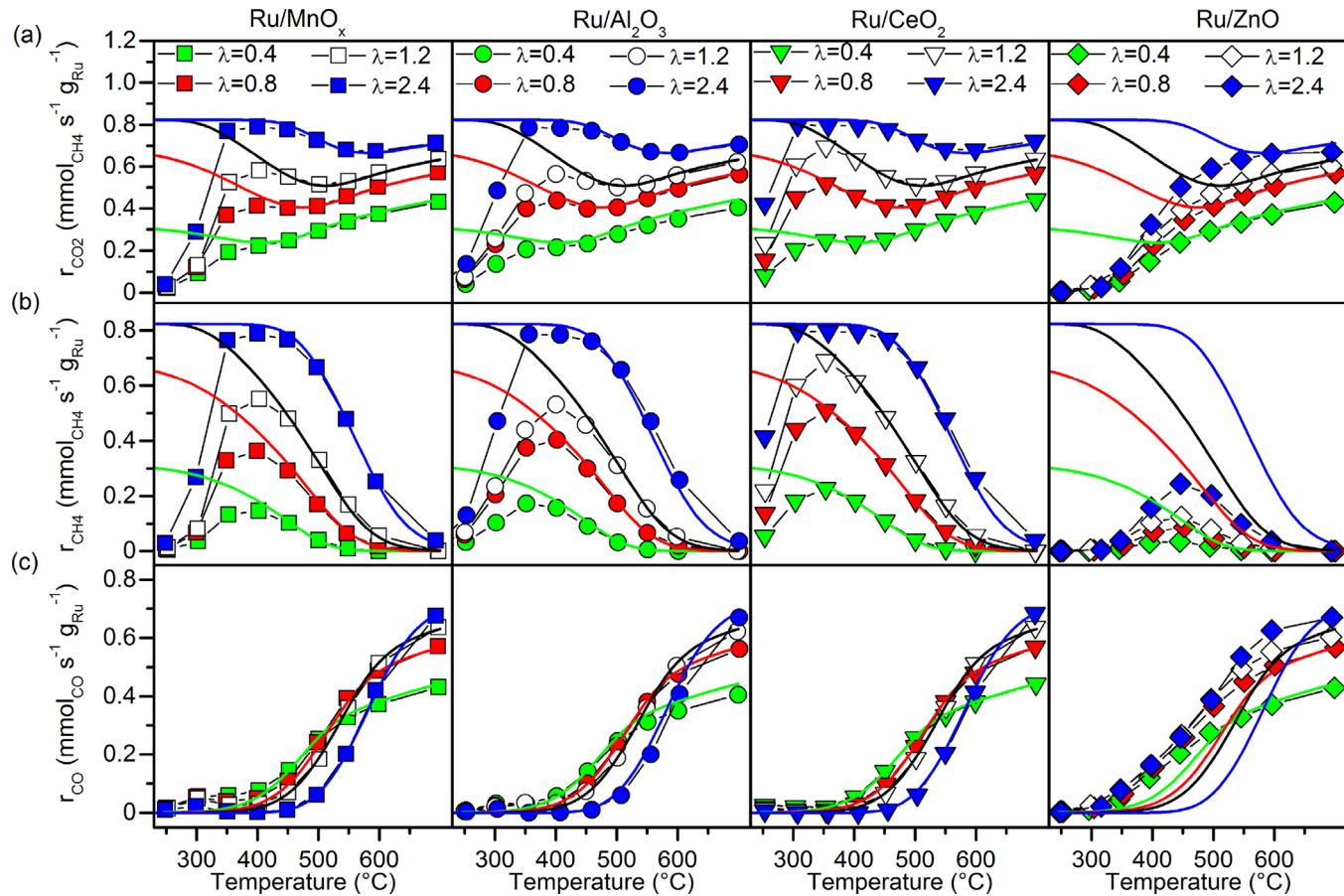


**Fig. 10.** The steady state rates of (a)  $\text{CO}_2$  conversion, (b)  $\text{CH}_4$  production and (c)  $\text{CO}$  production measured as a function of the equivalence ratios,  $\lambda$ , of 0.4, 0.8, 1.2 and 2.4 with a constant  $\text{CO}_2$  reactant concentration of 2.3%. Shown in solid lines are the thermodynamic equilibrium levels calculated by minimizing the Gibbs free energy.

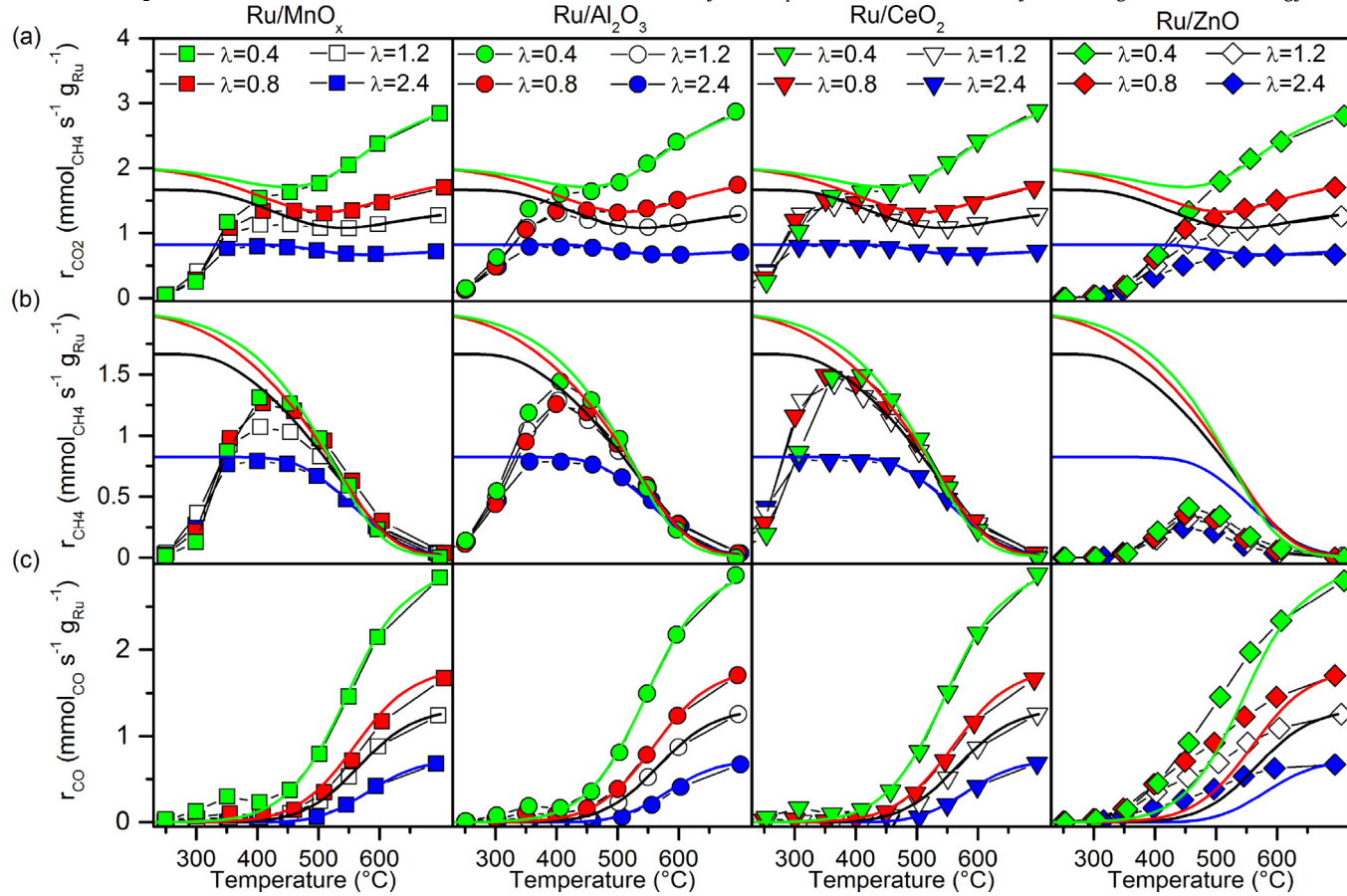


**Fig. 11.** The steady state rates of (a)  $\text{CO}_2$  conversion, (b)  $\text{CH}_4$  production and (c)  $\text{CO}$  production rates measured as a function of the equivalence ratios,  $\lambda$ ,

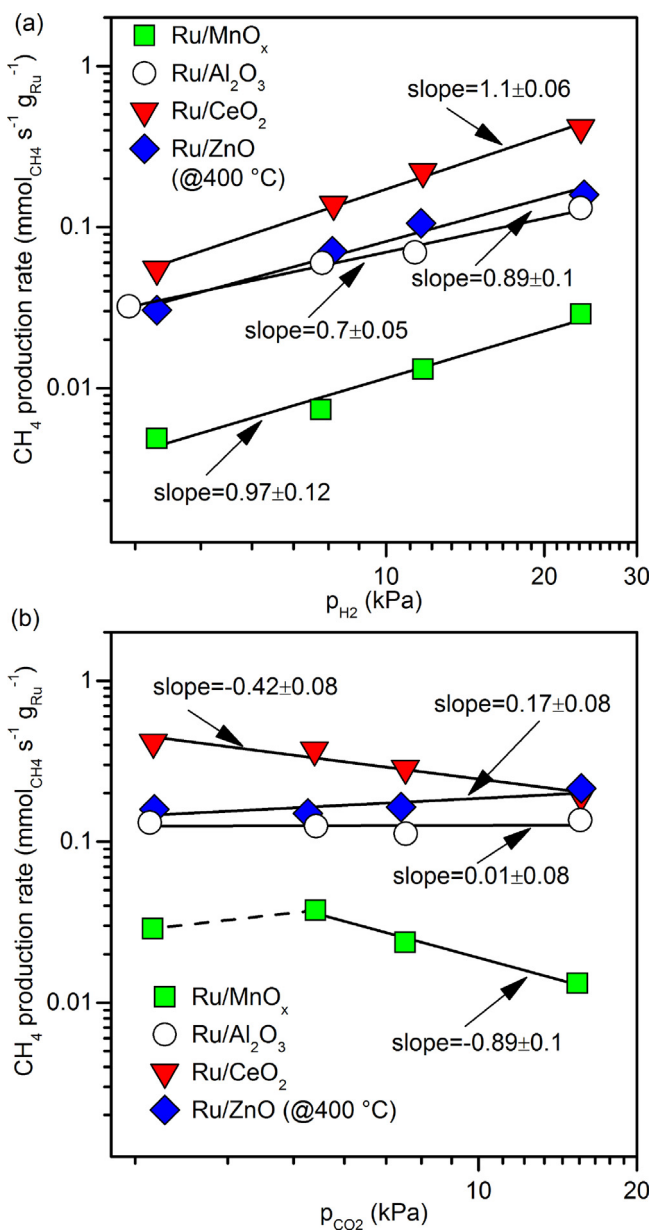


**Fig. 12.** The rates of methane production measured as a function of (a)  $\text{H}_2$  and (b)  $\text{CO}_2$  partial pressures over  $\text{Ru/MnO}_x$ ,  $\text{Ru/Al}_2\text{O}_3$ ,  $\text{Ru/CeO}_2$  and  $\text{Ru/ZnO}$ . The reaction temperature was  $250^\circ\text{C}$  except for  $\text{Ru/ZnO}$  which was  $400^\circ\text{C}$  due to low catalytic conversions.

$\text{Ru}$  by  $\text{CO}$  due to the stronger  $\text{Ru-CO}$  adsorption in case of irreducible supports. This would limit the sites for  $\text{H}_2$  dissociation and thus reduce the influence of the  $\text{H}_2$  partial pressure on the  $\text{CH}_4$  production rate. As shown in Fig. 12b, the dependency of  $\text{CH}_4$  production rates on  $\text{CO}_2$  concentration is more complex. The order of reaction with respect to  $\text{CO}_2$  ranges from slightly positive for  $\text{Ru/ZnO}$  ( $0.17 \pm 0.08$ ) to zero for  $\text{Ru/Al}_2\text{O}_3$  ( $0.01 \pm 0.08$ ) and negative for  $\text{Ru/CeO}_2$  ( $-0.42 \pm 0.08$ ) and  $\text{Ru/MnO}_x$  ( $-0.89 \pm 0.1$ ). The difference can be traced to the competitive Langmuir-type adsorption of the key intermediates  $\text{CO}^*$  and  $\text{H}^*$  on  $\text{Ru}$  as function of support reducibility (see  $\text{H}_{\text{ad}}/\text{CO}_{\text{ad}}$  ratios in Table 2). The  $\text{Ru/Al}_2\text{O}_3$  catalyst is expected to be quasi-saturated with  $\text{CO}$  even at low  $\text{CO}_2$  concentration due to the strong  $\text{Ru-CO}$  adsorption in case of irreducible

supports. Therefore, a change in  $\text{CO}_2$  partial pressure has no effect on the  $\text{CH}_4$  production rate and a zero reaction order is observed. For the reducible supports  $\text{CeO}_2$  and  $\text{MnO}_x$ , a larger number of  $\text{H}_2$  dissociation sites are available which are however lost at higher  $\text{CO}_2$  concentrations as reflected by the negative  $\text{CO}_2$  reaction order. For the  $\text{Ru/ZnO}$  catalyst, barely any  $\text{CO}$  adsorbs on  $\text{Ru}$  and larger  $\text{CO}_2$  concentrations are required to obtain appreciable amounts of  $\text{CO}^*$ .

### 3.3. *in situ* DRIFTS of catalytic $\text{CO}_2$ methanation

*In situ* DRIFTS were carried out to follow the speciation on the catalysts under reaction environment. Comparing the spectra of the as-synthesized and pretreated samples shows absorption peak around  $2130$ – $1780\text{ cm}^{-1}$  (Fig. S2). This peak only develops after  $\text{H}_2$  was introduced at elevated temperatures and disappears upon exposing the sample to air, suggesting that it may be related to the  $\text{Ru-O}$  overtone of some  $\text{RuO}_x\text{-OH}$  species [72,73]. A drastic decrease in the IR after the reduction of  $\text{Ru/ZnO}$  prevented acquisition of IR absorbance signal (Fig. S2d). Instead, the  $\text{Ru/ZnO}$  was only treated under  $\text{He}$  at the same temperature to remove any moisture and organic/carbonate impurities from the surface. The subsequent cooling of the catalyst to  $250^\circ\text{C}$  and the introduction of 1%  $\text{CO}_2$  saw the formation of bridged carbonates on  $\text{Ru/Al}_2\text{O}_3$  with peaks at  $3619$ ,  $1647$ ,  $1444$ , and  $1231\text{ cm}^{-1}$  (Fig. 13b) [60,61]. Additionally, a peak for the carbonyl on  $\text{Ru}$  can be seen at  $2066\text{ cm}^{-1}$  as well as significant amounts of  $\text{C-H}$  bonds (see  $2926$  and  $2857\text{ cm}^{-1}$  at  $t=0$  in Fig. 14b). The surface carbonyl reflects the dissociative adsorption of  $\text{CO}_2$  leading to  $\text{CO}$  on  $\text{Ru}$ , and the intensity scales qualitatively with the amount of chemisorbed  $\text{CO}$  seen earlier from the pulsed  $\text{CO}$  chemisorption (Table 2). The formed  $\text{C-H}$  bonds, combined with the peaks at  $1539$  and  $1331\text{ cm}^{-1}$ , can be assigned to bidentate formates, which are formed from the carbonation of the surface hydroxyl moieties [63,66]. The formation of formates were also recorded for  $\text{Ru/CeO}_2$  (Fig. 13c) and  $\text{Ru/MnO}_x$  (Fig. 13a). In both cases, the peaks at around  $850\text{ cm}^{-1}$  can be assigned to mono- or bidentate carbonates. As the  $\text{Ru/ZnO}$  sample was not reduced, only negligible amount of carbonyl on  $\text{Ru}$  can be detected at  $2026\text{ cm}^{-1}$ .

Subsequent co-introduction of  $\text{H}_2$  resulted in the catalyst reduction as seen by the decreasing valley at  $2130$ – $1780\text{ cm}^{-1}$  (Fig. 14a–c). The hydroxyl groups consumed during  $\text{CO}_2$  adsorption to form formates are regenerated and an increase in the  $\text{C-H}$  vibrational peak can be observed. Accordingly,  $\text{C-O}$  vibrational peaks assigned to formate species increase (Fig. 14a–c). A red shift in the IR absorbance peaks of carbonyl on  $\text{Ru}$  from  $2065\text{ cm}^{-1}$  for  $\text{Ru/Al}_2\text{O}_3$  to  $2057\text{ cm}^{-1}$  for  $\text{Ru/CeO}_2$  and  $2045\text{ cm}^{-1}$  for  $\text{Ru/MnO}_x$  can be observed (Fig. 14d). A red shift of the carbonyl peak was reported to be caused by decreasing coverage of  $\text{CO}$  on precious metals and the accompanied decrease of the dipole–dipole coupling of co-adsorbed  $\text{CO}$  molecules [74]. The expected  $\text{H}^*/\text{CO}^*$  surface coverage of  $\text{Ru}$  based on the measured  $\text{H}_{\text{ad}}/\text{CO}_{\text{ad}}$  ratio (Table 2) agrees well with a decreasing  $\text{CO}$  coverage from  $\text{Ru/Al}_2\text{O}_3$  to  $\text{Ru/CeO}_2$  to  $\text{Ru/MnO}_x$ . Removing  $\text{CO}_2$  from the  $\text{CO}_2/\text{H}_2/\text{He}$  gas mixture resulted in a gradual decrease of the carbonyl and carbonate/formate peaks (Fig. 15). Notably, the  $\text{C-H}$  peaks around  $3000$ – $2700\text{ cm}^{-1}$  remains almost unchanged. Most likely the  $\text{C-H}$  stretching peak is not only caused by the formate species but overlaps with adsorbed  $\text{CH}_2$  or  $\text{CH}_3$  [16]. Addition of  $\text{CO}_2$  into a  $\text{H}_2/\text{He}$  gas stream (Fig. S3) resulted in qualitatively similar DRIFTS peaks as  $\text{H}_2$  addition to a  $\text{CO}_2$  stream (Fig. 14), indicating that the sequence of introduced reactants has little influence on the formed intermediates/products.

of 0.4, 0.8, 1.2 and 2.4 and a constant  $\text{H}_2$  reactant concentration of 22%. Shown in solid lines are the thermodynamic equilibrium levels calculated by minimizing the Gibbs free energy.

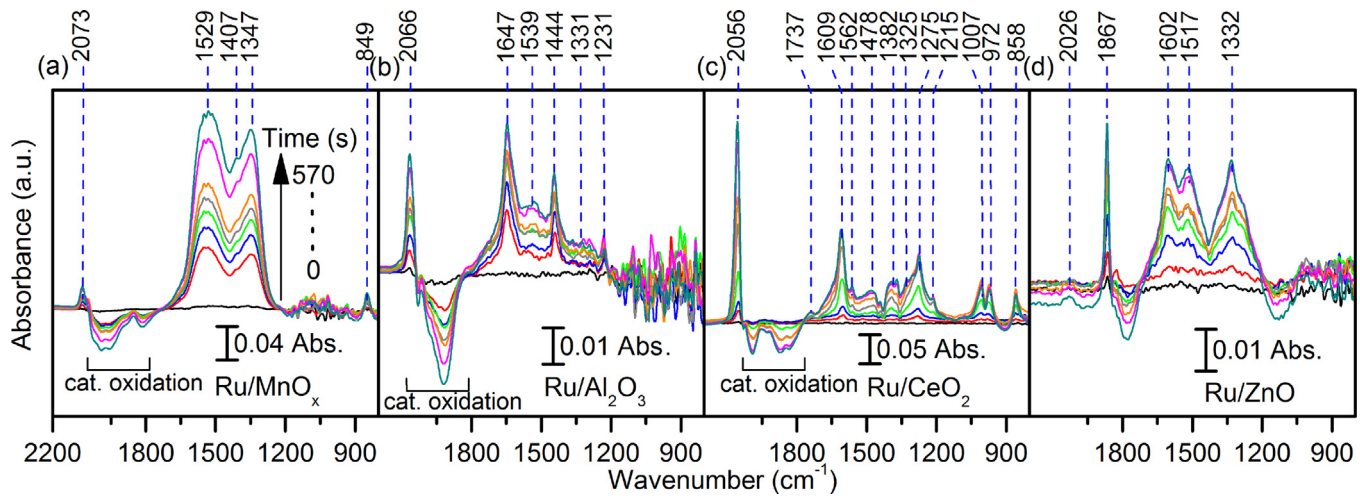


**Fig. 13.** Time-resolved DRIFT spectra of (a) Ru/MnO<sub>x</sub>, (b) Ru/Al<sub>2</sub>O<sub>3</sub>, (c) Ru/CeO<sub>2</sub> and (d) Ru/ZnO, upon the introduction of 1% CO<sub>2</sub>/He at 250 °C. The samples were pretreated at 350 °C with 10% H<sub>2</sub>/He (Ru/ZnO pure He) for 10 min and cooled to 250 °C under He flow.

#### 3.4. Reaction mechanism of CO<sub>2</sub> methanation

It is well established that the dissociative adsorption of CO<sub>2</sub> resulting in CO\* on Ru is the first reaction step of CO<sub>2</sub> methanation [16,18]. The CO\* is either further dissociated directly to form C\* and O\* followed by hydrogenation to CH<sub>x</sub>\*, or it dissociates with the assistance of H\* to form the hydroxylmethylene intermediate (HCOH\*) followed by abstraction of O to form CH<sub>x</sub>\* [16,20–23]. In both case, the catalytic reaction rate depends on the ease of C–O bond breaking and the ratio of co-adsorbed CO\* and H\*. The measured amounts of chemisorbed H<sub>2</sub> and CO (Table 2) and the observed red shift of the carbonyl peak (Fig. 14d) indi-

cated that Ru/Al<sub>2</sub>O<sub>3</sub> exhibits the highest Ru–CO coverage followed by Ru/CeO<sub>2</sub>, Ru/MnO<sub>x</sub>, and Ru/ZnO. The change in Ru–CO surface coverage hereby agrees with the support reducibility (Fig. 2). The reduced Ru–CO coverage can be explained by the reported weaker electron back-donation from precious metals to the  $\pi^*$  orbital of CO and consequently weaker Ru–CO adsorption strength upon oxide support reduction [69,70]. Even though the C–O bond strength was not measured directly in this study, a change in the back-donation is expected to also alter the C–O bond. The reduction of the oxide support would cause a lower electron density in the anti-bonding  $\pi^*$  orbital of CO, which would translate into a stronger C–O bond. Based on the above considerations it is expected that slightly

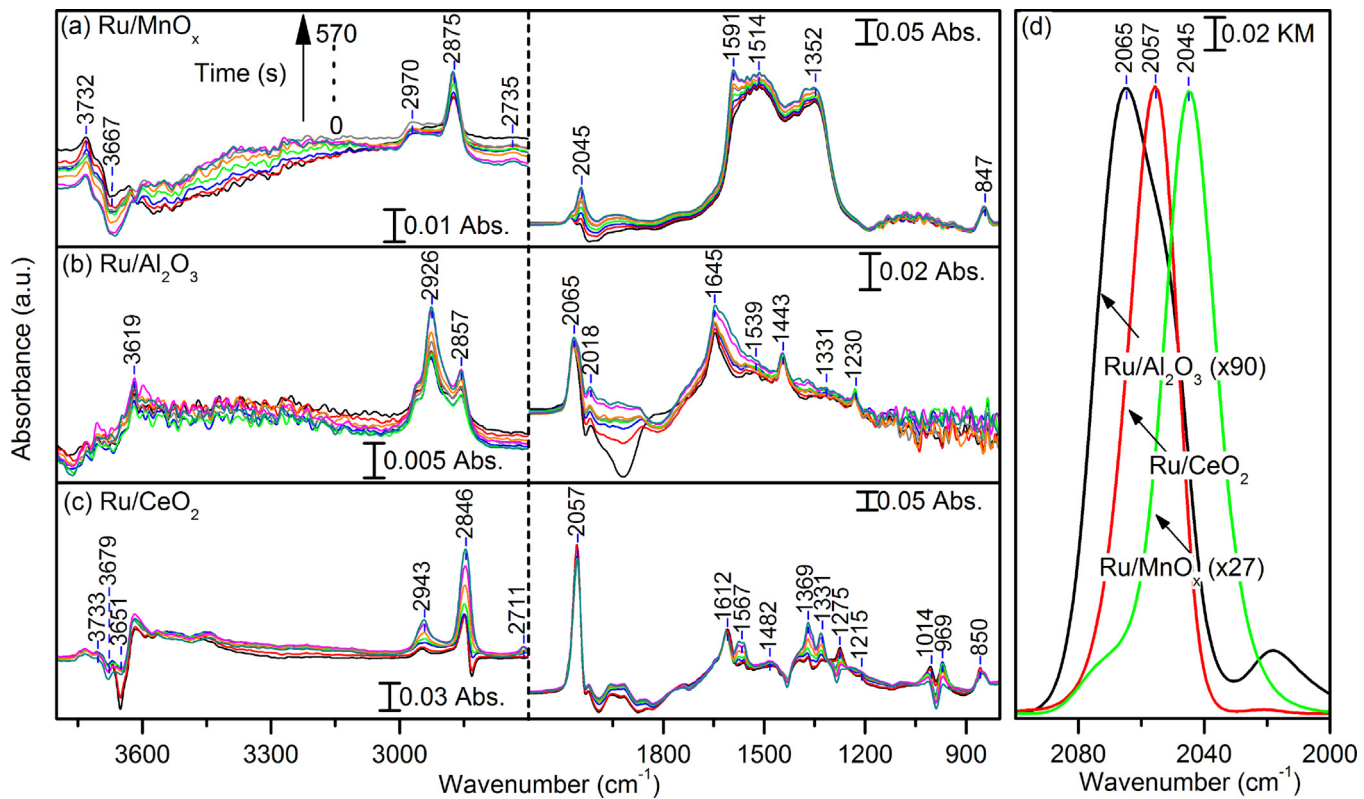


**Fig. 14.** Time-resolved DRIFT spectra of (a) Ru/MnO<sub>x</sub>, (b) Ru/Al<sub>2</sub>O<sub>3</sub> and (c) Ru/CeO<sub>2</sub>, upon the introduction of 3.2% H<sub>2</sub> into the 1% CO<sub>2</sub>/He at 250 °C. Shown in (d) is the corresponding carbonyl region for Ru/MnO<sub>x</sub>, Ru/Al<sub>2</sub>O<sub>3</sub> and Ru/CeO<sub>2</sub>.

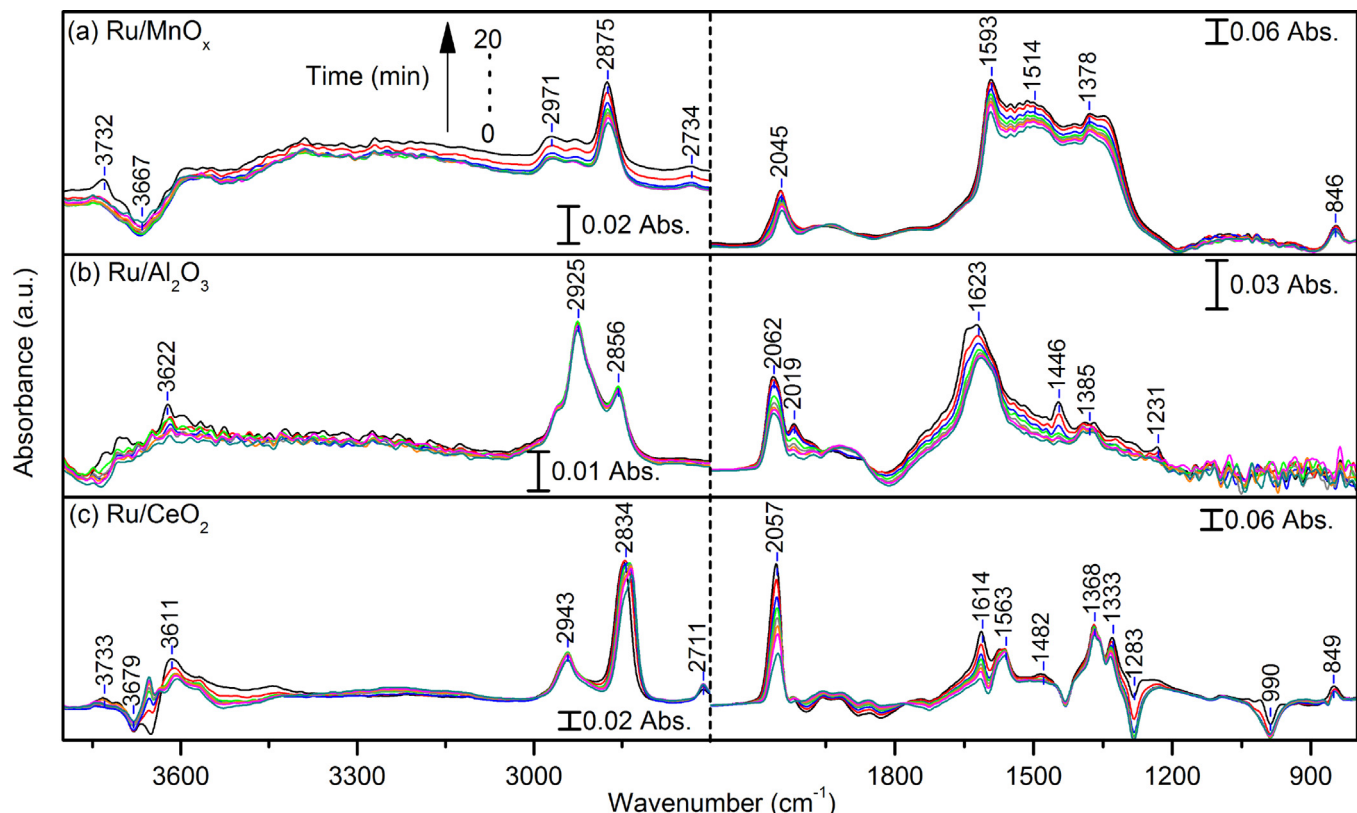


**Fig. 15.** Time-resolved DRIFT spectra of (a) Ru/MnO<sub>x</sub>, (b) Ru/Al<sub>2</sub>O<sub>3</sub> and (c) Ru/CeO<sub>2</sub>, upon the removing of CO<sub>2</sub> from the preceding gas mixture of 1% CO<sub>2</sub>/3.2% H<sub>2</sub>/He at 250 °C.

reducible support resulting in an increased number of H<sub>2</sub> dissociation sites on Ru due to weaker CO adsorption but still sufficiently weak C–O bonds would result in the highest catalytic activity. CeO<sub>2</sub> is such a support and an excellent CO<sub>2</sub> conversion and CH<sub>4</sub> selectivity was observed for the Ru/CeO<sub>2</sub> catalyst (Fig. 8).

#### 4. Conclusions

Flame spray pyrolysis was used for the synthesis of supported Ru nanoparticles and the influence of the metal oxide support on the catalytic methanation of CO<sub>2</sub> was investigated. The catalytic activity of the pristine oxide supports (Al<sub>2</sub>O<sub>3</sub>, CeO<sub>2</sub>, MnO<sub>x</sub>, and ZnO) was directly linked to the strength of basic sites, which resulted in large amounts of CO formed through the reverse water-gas shift reaction. However, no significant CH<sub>4</sub> formation was observed due to the absence of H<sub>2</sub> dissociation sites. The addition of Ru provided such sites and resulted in a high CO<sub>2</sub> conversion at low temperatures with CH<sub>4</sub> selectivities up to 95–100%. A thorough reaction kinetic analysis combined with quantitative gas chemisorption and *in situ* DRIFTS revealed that an enhanced support reducibility decreased the Ru–CO coverage. The reduced CO coverage increased the number of H<sub>2</sub> dissociation sites but in turn is expected to strengthened the C–O bonds due to a lower electron density in the  $\pi^*$  antibonding orbital of CO. Hence, the CO<sub>2</sub> methanation on supported Ru requires a delicate tuning of the Ru–CO adsorption strength to obtain sites for H<sub>2</sub> dissociation while avoiding excessive strengthening of the C–O bond.

#### Acknowledgements

JAHD thanks the Research Grant Council of Hong Kong for awarding the Hong Kong PhD Fellowship Scheme. The work was financially supported by the Research Grant Council of Hong Kong

through the General Research Funds (Project 11302714). We thank Dr. Davide Ferri for support with the DRIFT spectra interpretation.

#### Appendix A. Supplementary data

Supplementary data associated with this article can be found, in the online version, at <http://dx.doi.org/10.1016/j.apcatb.2017.08.011>.

#### References

- [1] J. Hansen, M. Sato, P. Kharecha, D. Beerling, R. Berner, V. Masson-Delmotte, M. Pagani, M. Raymo, D.L. Royer, J.C. Zachos, *Open Atmos. Sci. J.* 2 (2008) 217–231.
- [2] P.M. Cox, R.A. Betts, C.D. Jones, S.A. Spall, I.J. Totterdell, *Nature* 408 (2000) 184–187.
- [3] S. Shafiee, E. Topal, *Energy Policy* 37 (2009) 181–189.
- [4] K. Aleklett, M. Höök, K. Jakobsson, M. Lardelli, S. Snowden, B. Soderbergh, *Energy Policy* 38 (2010) 1398–1414.
- [5] F.R. Pazheri, M.F. Othman, N.H. Malik, *Renewable Sustainable Energy Rev.* 31 (2014) 835–845.
- [6] G.A. Olah, G.K.S.P. Prakash, A. Goeppert, *J. Am. Chem. Soc.* 133 (2011) 12881–12898.
- [7] Y. Yan, Y. Dai, H. He, Y. Yu, Y. Yang, *Appl. Catal. B* 196 (2016) 108–116.
- [8] S. Eckle, M. Augustin, H.-G. Anfang, R.J. Behm, *Catal. Today* 181 (2012) 40–51.
- [9] J.H. Kwak, L. Kovarik, J. Szanyi, *ACS Catal.* 3 (2013) 2449–2455.
- [10] W. Wang, S. Wang, X. Ma, J. Gong, *Chem. Soc. Rev.* 40 (2011) 3703–3727.
- [11] J. Polanski, T. Siudyga, P. Bartczak, M. Kapkowski, W. Ambrozkiewicz, A. Nobis, R. Sitko, J. Klimontko, J. Szade, J. Lelatko, *Appl. Catal. B* 206 (2017) 16–23.
- [12] C. de Leitenburg, A. Trovarelli, J. Kašpar, *J. Catal.* 166 (1997) 98–107.
- [13] S. Sciré, C. Crisafulli, R. Maggiore, S. Minicó, S. Galvagno, *Catal. Lett.* 51 (1998) 41–45.
- [14] J. Gao, Q. Liu, F. Gu, B. Liu, Z. Zhong, F. Su, *RSC Adv.* 5 (2015) 22759–22776.
- [15] A. Beuls, C. Swalus, M. Jacquemin, G. Heyen, A. Karelovic, P. Ruiz, *Appl. Catal. B* 113–114 (2012) 2–10.
- [16] S. Eckle, H.-G. Anfang, R.J. Behm, *J. Phys. Chem. C* 115 (2011) 1361–1367.
- [17] A. Karelovic, P. Ruiz, *J. Catal.* 301 (2013) 141–153.
- [18] I.A. Fisher, A.T. Bell, *J. Catal.* 162 (1996) 54–65.
- [19] F. Solymosi, A. Erdőhelyi, T. Básági, *J. Catal.* 68 (1981) 371–382.
- [20] G. Weatherbee, C.H. Bartholomew, *J. Catal.* 87 (1984) 352–362.
- [21] S. Shetty, A.P.J. Jansen, R. A. van Santen, *J. Am. Chem. Soc.* 131 (2009) 12874–12875.

[22] O.R. Inderwildi, S.J. Jenkins, D.A. King, *Angew. Chem. Int. Ed.* **47** (2008) 5253–5255.

[23] O.R. Inderwildi, S.J. Jenkins, D.A. King, *J. Phys. Chem. C* **112** (2008) 1305–1307.

[24] A. Karelovic, P. Ruiz, *Appl. Catal. B* **113–114** (2012) 237–249.

[25] X. Wang, H. Shi, J.H. Kwak, J. Szanyi, *ACS Catal.* **5** (2015) 6337–6349.

[26] T. Mori, H. Masuda, H. Imai, *J. Mol. Catal.* **25** (1984) 263–271.

[27] R. Büchel, A. Baiker, S.E. Pratsinis, *Appl. Catal. A* **277** (2014) 93–101.

[28] Z.L. Zhang, A. Kladi, X.E. Verykios, *J. Catal.* **156** (1995) 37–50.

[29] J.-N. Park, E.W. McFarland, *J. Catal.* **266** (2009) 92–97.

[30] J.A.H. Dreyer, H.K. Grossmann, J. Chen, T. Grieb, B.B. Gong, P.H.-L. Sit, L. Mädler, W.Y. Teoh, *J. Catal.* **329** (2015) 248–261.

[31] W.Y. Teoh, R. Amal, L. Mädler, *Nanoscale* **2** (2010) 1324–1347.

[32] R. Strobel, S.E. Pratsinis, *J. Mater. Chem.* **17** (2007) 4743–4756.

[33] R. Strobel, A. Baiker, S.E. Pratsinis, *Adv. Powder Technol.* **17** (2006) 457–480.

[34] G. Busca, *Phys. Chem. Chem. Phys.* **1** (1999) 723–736.

[35] P. Hohenberg, W. Kohn, *Phys. Rev.* **136** (1964) B864–B871.

[36] W. Kohn, L.J. Sham, *Phys. Rev.* **140** (1965) A1133–A1138.

[37] P. Giannozzi, S. Baroni, N. Bonini, M. Calandra, R. Car, C. Cavazzoni, D. Ceresoli, G.L. Chiarotti, M. Cococcioni, I. Dabo, A. Dal Corso, S. de Gironcoli, S. Fabris, G. Fratesi, R. Gebauer, U. Gerstmann, C. Gougaudis, A. Kokalj, M. Lazzeri, L. Martin-Samos, N. Marzari, F. Mauri, R. Mazzarello, S. Paolini, A. Pasquarello, L. Paulatto, C. Sbraccia, S. Scandolo, G. Scalauzero, A.P. Seitsonen, A. Smogunov, P. Umari, R.M. Wentzcovitch, *J. Phys. Condens. Matter* **21** (2009) 395502.

[38] J.P. Perdew, K. Burke, M. Ernzerhof, *Phys. Rev. Lett.* **77** (1996) 3865–3868.

[39] D. Vanderbilt, *Phys. Rev. B* (1990) 7892–7895.

[40] L. Li, X. Feng, Y. Nie, S. Chen, F. Shi, K. Xiong, W. Ding, X. Qi, J. Hu, Z. Wei, L.-J. Wan, M. Xia, *ACS Catal.* **5** (2015) 4825–4832.

[41] M. Digne, P. Sautet, P. Raybaud, P. Euzen, H. Toulhoat, *J. Catal.* **226** (2004) 54–68.

[42] V. Fernandes, R.J.O. Mossanek, P. Schio, J.J. Klein, A.J.A. de Oliveira, W.A. Ortiz, N. Mattoso, J. Varalda, W.H. Schreiner, M. Abbate, D.H. Mosca, *Phys. Rev. B* **80** (2009) 035202.

[43] E.H. Kisi, M.M. Elcombe, *Acta Cryst.* **45** (1989) 1867–1870.

[44] B. Wang, M.-L. Bocquet, S. Marchini, S. Günther, J. Wintterlin, *Phys. Chem. Chem. Phys.* **10** (2008) 3530–3534.

[45] J. Karthikeyan, C.C. Berndt, J. Tikkkanen, J.Y. Wang, A.H. King, H. Herman, *Nanostruct. Mater.* **8** (1997) 61–74.

[46] Y.N. Ko, S.B. Park, S.H. Choi, Y.C. Kang, *Sci. Rep.* **4** (2014) 5751.

[47] R. Strobel, W.J. Stark, L. Mädler, S.E. Pratsinis, A. Baiker, *J. Catal.* **213** (2003) 296–304.

[48] R. Strobel, F. Krumeich, W.J. Stark, S.E. Pratsinis, A. Baiker, *J. Catal.* **222** (2004) 307–314.

[49] L. Mädler, W.J. Stark, S.E. Pratsinis, *J. Mater. Res.* **17** (2002) 1356–1362.

[50] T. Tani, L. Mädler, S.E. Pratsinis, *J. Nanopart. Res.* **4** (2002) 337–343.

[51] K. Hembram, D. Sivaprakasam, T.N. Rao, K. Wegner, *J. Nanopart. Res.* **15** (2013) 1461.

[52] M. Tepluchin, D.K. Pham, M. Casapu, L. Mädler, S. Kuretic, J.-D. Grunwaldt, *Catal. Sci. Technol.* **5** (2015) 455–464.

[53] S. Wagloehner, M. Nitzer-Noski, S. Kureti, *J. Chem Eng.* (2015) 492–504.

[54] T. Désaunay, G. Bonura, V. Chioldo, S. Freni, J.-P. Couzinié, J. Bourgon, A. Ringuedé, F. Labat, C. Adamo, M. Cassir, *J. Catal.* **297** (2013) 193–201.

[55] Y. Gao, W. Wang, S. Chang, W. Huang, *ChemCatChem* **5** (2013) 3610–3620.

[56] L. Wang, G. Lu, D. Yang, J. Wang, Z. Zhu, Z. Wang, K. Zhou, *ChemCatChem* **5** (2013) 1308–1312.

[57] M.A. Aramendia, V. Borau, C. Jiménez, F. Lafont, J.M. Marinas, A. Porras, F.J. Urbano, *Rapid Commun. Mass Spectrom.* **9** (1995) 193–198.

[58] M.A. Aramendia, V. Borau, C. Jiménez, A. Marinas, J.M. Marinas, J.R. Ruiz, F.J. Urbano, *J. Mol. Catal. A: Chem.* **218** (2004) 81–90.

[59] T. Jin, T. Okuhara, G.J. Mains, J.M. White, *J. Phys. Chem.* **91** (1987) 3310–3315.

[60] J. Baltrusaitis, J. Schuttlefield, E. Zeitler, V.H. Grassian, *J. Chem Eng.* **170** (2011) 471–481.

[61] J. Baltrusaitis, J.H. Jensen, V.H. Grassian, *J. Phys. Chem. B* **110** (2006) 12005–12016.

[62] J. Szanyi, J.H. Kwak, *Phys. Chem. Chem. Phys.* **16** (2014) 15117–15125.

[63] Y. Denkwitz, A. Karpenko, V. Plzak, R. Leppelt, B. Schumacher, R.J. Behm, *J. Catal.* **246** (2007) 74–90.

[64] M.-F. Luo, Y.-J. Zhong, B. Zhu, X.-X. Yuan, X.-M. Zheng, *Appl. Surf. Sci.* **115** (1997) 185–189.

[65] L. Li, L. Song, H. Wang, C. Chen, Y. She, Y. Zhan, X. Lin, Q. Zheng, *Int. J. Hydrogen Energy* **36** (2011) 8839–8849.

[66] S.R. Tong, L.Y. Wu, M.F. Ge, W.G. Wang, Z.F. Pu, *Atmos. Chem. Phys.* **10** (2010) 7561–7574.

[67] T.V. Choudhary, C. Sivadinayara, D.W. Goodman, *Catal. Lett.* **72** (2001) 197–201.

[68] M.C.J. Bradford, P.E. Fanning, M.A. Vannice, *J. Catal.* **172** (1997) 479–484.

[69] M. Liang, X. Wang, H. Liu, H. Liu, Y. Wang, *J. Catal.* **255** (2008) 335–342.

[70] C. Xiao, M. Liang, A. Gao, J. Xie, Y. Wang, H. Liu, *J. Nanopart. Res.* **15** (2013) 1822.

[71] M. Kusmierz, *Catal. Today* **137** (2008) 429–432.

[72] C. Mondelli, D. Ferri, A. Baiker, *J. Catal.* **258** (2008) 170–176.

[73] Z. Opre, J.-D. Grunwaldt, M. Maciejewski, D. Ferri, T. Mallat, A. Baiker, *J. Catal.* **230** (2005) 406–419.

[74] M. Primet, *J. Catal.* **88** (1984) 273–282.